Supplementary Materials

S. Abrahamyan

Yerevan Physics Institute, Yerevan, Armenia

Z. Ahmed, R. S. Holmes, C.-M. Jen, A. Rakhman, P. A. Souder,* and L. Zana

Syracuse University, Syracuse, New York 13244, USA

H. Albataineh, A. Etile, E. Gasser, and F. Itard

Laboratoire de Physique Corpusculaire,

Clermont-Ferrand Campus des Czeaux, 63171 Aubire Cedex, France

K. Aniol and D.J. Margaziotis

California State University, Los Angeles,

Los Angeles, California 90032, USA

D. S. Armstrong, T. Averett, J. Hoskins, E. Jensen, and J. Leckey IV

College of William and Mary, Williamsburg, Virginia 23187, USA

W. Armstrong, D. Flay, Z.-E. Meziani, M. Posik, and H. Yao

Temple University, Philadelphia, Pennsylvania 19122, USA

B. Babineau, T. Holmstrom, A. Palmer, and W. Troth

Longwood University, Farmville, Virginia 23909, USA

A. Barbieri, G. D. Cates, M. M. Dalton, X. Deng, C. Gu, G. Jin,

R. Lindgren, N. Liyanage, V. Nelyubin, K. D. Paschke, S. Riordan,

K. Saenboonruang, R. Silwal, R. Subedi, W. A. Tobias, D. Wang, and X. Zheng

University of Virginia, Charlottesville, Virginia 22903, USA

V. Bellini, A. Giusa, G. Russo, M. L. Sperduto, and C. M. Sutera

INFN, Dipt. di Fisica dell'Univ. di Catania, I-95123 Catania, Italy

R. Beminiwattha, P.M. King, and B. Waidyawansa

Ohio University, Athens, Ohio 45701, USA

J. Benesch, A. Camsonne, J.-P. Chen, A. Deur, J. Gomez, J. Grames,
O. Hansen, J. Hansknecht, D. W. Higinbotham, J. J. LeRose,
A. McCreary, R. W. Michaels, S. Nanda, B. Poelker, A. Saha,[†]
B. Sawatzky, P. Solvignon, R. Suleiman, B. Wojtsekhowski, and J. Zhang
Thomas Jefferson National Accelerator Facility,
Newport News, Virginia 23606, USA

F. Benmokhtar and P. Carter
Christopher Newport University, Newport News, Virginia 23606, USA

T. Bielarski, S. K. Phillips, and K. Slifer
University of New Hampshire, Durham, New Hampshire 03824, USA

W. Boeglin and P. Markowitz
Florida International University, Miami, Florida 33199, USA

M. Canan
Old Dominion University, Norfolk, Virginia 23529, USA

C. Chen
Hampton University, Hampton, Virginia 23668, USA

O. Hen and K. Kliakhandler
Tel Aviv University, P.O. Box 39040, Tel-Aviv 69978, Israel

F. Cusanno,[‡] S. Frullani, F. Garibaldi, and F. Mammoliti
INFN, Sezione di Roma, gruppo Sanità, I-00161 Rome, Italy

R. De Leo
INFN, Sezione di Bari and University of Bari, I-70126 Bari, Italy

K. de Jager
Thomas Jefferson National Accelerator Facility,
Newport News, Virginia 23606, USA and
University of Virginia, Charlottesville, Virginia 22903, USA

W. Deconinck

Massachusetts Institute of Technology,

Cambridge, Massachusetts 02139, USA and

College of William and Mary, Williamsburg, Virginia 23187, USA

P. Decowski

Smith College, Northampton, Massachusetts 01063, USA

D. Dutta and N. Nuruzzaman

Mississippi State University, Mississippi State, Mississippi 39762, USA

G. B. Franklin, M. Friend, D. Parno, and B. Quinn

Carnegie Mellon University, Pittsburgh, Pennsylvania 15213, USA

E. Fuchey

Clermont Université, Université Blaise Pascal,

CNRS/IN2P3, Laboratoire de Physique Corpusculaire,

FR-63000 Clermont-Ferrand, France and

Temple University, Philadelphia, Pennsylvania 19122, USA

R. Gilman and Y. Zhang

Rutgers University, The State University of New Jersey,

New Brunswick, New Jersey 08901, USA

A. Glamazdin and R. Pomatsalyuk

Kharkov Institute of Physics and Technology, Kharkov 61108, Ukraine

C. J. Horowitz

Indiana University, Bloomington, Indiana 47405, USA

J. Huang, A. Kelleher, S. Kowalski, N. Muangma, and V. Sulkosky

Massachusetts Institute of Technology,

Cambridge, Massachusetts 02139, USA

C. E. Hyde

Old Dominion University, Norfolk, Virginia 23529, USA and
Clermont Université, Université Blaise Pascal,
CNRS/IN2P3, Laboratoire de Physique Corpusculaire,
FR-63000 Clermont-Ferrand, France

S. Johnston, K. S. Kumar, J. Mammei, D. McNulty,
L. Mercado, P. Rogan, J. Wexler, and V. Yim
University of Massachusetts Amherst,
Amherst, Massachusetts 01003, USA

J. Leacock
Virginia Polytechnic Institute and State University, Blacksburg, Virginia 24061, USA

J. H. Lee
College of William and Mary, Williamsburg, Virginia 23187, USA and
Ohio University, Athens, Ohio 45701, USA

N. Lubinsky
Rensselaer Polytechnic Institute, Troy, New York 12180, USA

M. Mihovilovic and S. Sirca
Institut Jožef Stefan, 3000 SI-1001 Ljubljana, Slovenia

C. Muñoz-Camacho
Clermont Université, Université Blaise Pascal,
CNRS/IN2P3, Laboratoire de Physique Corpusculaire,
FR-63000 Clermont-Ferrand, France

Y. Oh
Seoul National University, Seoul 151-742, South Korea

A.J.R. Puckett
Los Alamos National Laboratory, Los Alamos, New Mexico 87545, USA

P. E. Reimer and X. Zhan

Argonne National Laboratory, Argonne, Illinois 60439, USA

G. Ron

Lawrence Berkeley National Laboratory, Berkelery, California 94720, USA

A. Shahinyan

Yerevan Physics Institute, Yerevan, Armenia and
Thomas Jefferson National Accelerator Facility,
Newport News, Virginia 23606, USA

G. M. Urciuoli

INFN, Sezione di Roma, I-00161 Rome, Italy

R. Wilson

Harvard University, Cambridge, Massachusetts 02138, USA

X. Yan, Y. Ye, and P. Zhu

University of Science and Technology of China, Hefei, Anhui 230026, P.R. China

Z. Ye

Hampton University, Hampton, Virginia 23668, USA and
University of Virginia, Charlottesville, Virginia 22903, USA

(Dated: September 26, 2012)

PACS numbers: 21.10.Gv, 21.65.Ef, 25.30.Bf, 27.80.+w $190 \leq A \leq 219$

*Electronic address: `souder@physics.syr.edu`

†Deceased

‡now at Technische Universitaet Muenchen, Excellence Cluster Universe, Garching b. Muenchen, Germany

Draft version: to supplement Science article

I. APPARATUS

The experimental techniques for measuring small asymmetries of order 1 ppm have been successfully deployed in parity experiments at electron scattering facilities [**?**]-[**?**]. The recent experiments at Jefferson Lab, such as HAPPEX [**?**] and PREX [**?**] have maintain systematic errors associated with helicity reversal at the 10^{-8} level. The asymmetries sought for in this experiment are of order 100 ppm with accuracies of about 1 ppm, which is two orders-of-magnitude above the established systematic error.

A significant challenge of the measurement is to separate electrons from the charged pion background that arise from electro- or photo-productions. While the standard HRS detector package and data acquisition (DAQ) system routinely provide such a high particle identification (PID) performance, they are based on full recording of the detector signals and are limited to event rates up to 4 kHz. This is not sufficient for the few-hundred kHz rates for the experiment. Thus we have built new DAQ designed to count event rates up to 1 MHz with hardware-based particle identification [**?**].

The main parts of the apparatus will be described in this section. These include the polarized electron beam, the beam monitors, the spectrometers and detectors, the data acquisition system, and the beam polarimeters.

A. Polarized Electron Beam

The electron beam originated from a GaAs photocathode illuminated by circularly polarized light [35]. By reversing the sign of the laser circular polarization, the direction of the spin at the target could be reversed rapidly [36]. A half-wave ($\lambda/2$) plate was periodically inserted into the laser optical path which passively reversed the sign of the electron beam polarization. Roughly equal statistics were thus accumulated with opposite signs for the measured asymmetry, which suppressed many systematic effects. The direction of the polarization could be controlled by a Wien filter and solenoidal lenses near the injector [**?**]. The accelerated beam was directed into Hall A, where its intensity, energy and trajectory on target were inferred from the response of several monitoring devices.

Each period of constant spin direction is referred to as a "window". The beam monitors, target, detector components and electronics were designed so that the fluctuations in the fractional difference in the PMT response between a pair of successive windows were dominated by scattered electron counting statistics. To keep spurious beam-induced asymmetries under control at well below the ppm level, careful attention was given to the design and configuration of the laser optics leading to the photocathode [36].

The spin-reversal rate was 30 Hz. The integrated response of each detector PMT and beam monitor was digitized and recorded for each window. The raw spin-direction asymmetry A_{raw} in each spectrometer arm was computed from the the detector response normalized to the beam intensity for each window pair. The sequence of these patterns was chosen with a pseudorandom number generator.

B. Beam Monitoring

Helicity-correlations in the beam properties such as energy and position are a primary concern for parity-violation experiments. At Jefferson Lab, the beam position is measured by "stripline" monitors [**?**], each of which consists of a set of four thin wires placed symmetrically around the beam pipe. The wires act as antennae that provide a signal (modulated by the microwave structure of the electron beam) proportional to the beam position as well as intensity. Figure 1 shows the correlation between the measured position at a BPM near the target compared with the predicted position using neighboring BPMs for a beam current of 100 μA (2×10^{13} electrons per window). A precision for $\delta(\Delta X_i)$ close to 1 μm was obtained for the average beam position for a beam window containing 2×10^{13} electrons.

To measure the beam intensity, microwave cavity BCMs have been developed at Jefferson Lab [**?**]. The precision $\delta(A_I)$ that has been achieved for a 30 ms beam window at 100 μA is 4×10^{-5}. This superior resolution is a result of good radiofrequency (rf) instrumentation as well as a high resolution 18-bit ADC, which will be discussed in section **??**.

Let the detected scattered flux of electrons be D in each spectrometer, and the beam current I, measured independently for every window by integrating the signals over the helicity period. From these we obtained the normalized flux $d_i \equiv D_i/I_i$ and the cross section asymmetry $(A_d)_i$ for the ith window pair. The raw asymmetry was then obtained

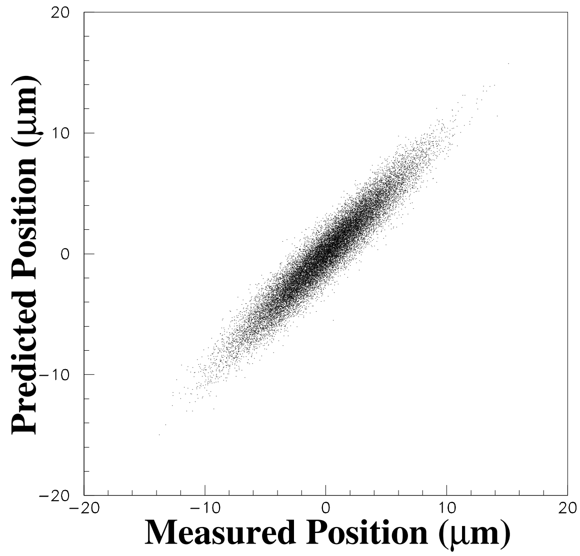

FIG. 1: Window-to-window beam jitter as measured by a BPM is plotted along the x axis. On the y axis is plotted the beam position as predicted by nearby BPMs. The residuals are smaller than 1 μm.

by appropriate averaging of N measurements:

$$(A_d)_i \equiv \left(\frac{d^+ - d^-}{d^+ + d^-}\right)_i \equiv \left(\frac{\Delta d}{2d}\right)_i$$
$$\delta(A_d) = \sigma(A_d)/\sqrt{N}. \tag{1}$$

where + and − denote the two helicity states in a pair.

A major goal of the experimental design is to $\sigma(A_d)$ should be dominated by the counting statistics in the scattered flux. As shown by fig N in ref [**?**], this goal was met.

There are two key parameters for each experimentally measured quantity M, such as detector rate, beam intensity, or beam position. The first is $\sigma(\Delta M)$, the size of the relative window pair-to-window pair fluctuations in $\Delta M \equiv M_+ - M_-$, which is affected by real fluctuations in the electron flux. The second is $\delta(\Delta M)$, the relative accuracy with which the window pair differences in M can be measured compared to the true value, which is dominated by instrumentation noise.

If $\sigma(\Delta M)$ is large enough, it might mean that there are non-statistical contributions to $\sigma(A_d)$ so that the latter is no longer dominated by counting statistics. In this case, it is crucial that $\delta(\Delta M) \ll \sigma(\Delta M)$ so that window pair to window pair corrections for the fluctuations in ΔM can be made.

As stated in **??**, we desire that $\sigma(A_d)$ be dominated by counting statistics. An example of possible non-statistical contributions is window-to-window relative beam intensity fluctuations, $\sigma(A(I)) \equiv \sigma(\Delta I/2I)$, which were observed to vary between 2×10^{-4} and 2×10^{-3}, depending on the quality of the laser and the beam tune. This is remarkable and a unique feature of the beam at Jefferson lab, since $\sigma(A_I) < \sigma(A_d)$. Nevertheless, the detector-intensity correlation can be exploited to remove the dependence of beam charge fluctuations on the measured asymmetry:

$$(A_d)_i \simeq \left(\frac{\Delta D}{2D} - \frac{\Delta I}{2I}\right)_i \equiv (A_D - A_I)_i. \tag{2}$$

(This is equation 1 to first order.)

Similarly, $\sigma(A_d)$ might be affected by random beam fluctuations in energy, position and angle. The corrections can be parameterized as follows:

$$(A_d^{\mathrm{corr}})_i = \left(\frac{\Delta D}{2D} - \frac{\Delta I}{2I}\right)_i - \sum_j (\alpha_j(\Delta X_j)_i). \tag{3}$$

Here, X_j are beam parameters such as energy, position and angle and $\alpha_j \equiv \partial D/\partial X_j$ are coefficients that depend on the kinematics of the specific reaction being studied, as well as the detailed spectrometer and detector geometry of the experiment.

By judicious choices of beam position monitoring devices (BPMs) and their respective locations, several measurements of beam position can be made from which the average relative energy, position, and angle of approach of each ensemble of electrons in a helicity window on target can be inferred. One can then write

$$(A_d^{\mathrm{corr}})_i = \left(\frac{\Delta D}{2D} - \frac{\Delta I}{2I}\right)_i - \sum_j (\beta_j(\Delta M_j)_i). \tag{4}$$

Here M_i are a set of 5 BPMs that span the parameter space of energy, position, and angle on target, and $\beta_i \equiv \partial D/\partial M_i$. It is worth noting that this approach of making corrections window by window automatically accounts for occasional random instabilities in the accelerator (such as klystron failures) that are characteristic of normal running conditions.

During our experiment run, we found that $\sigma(\Delta M_j)$ varied between 1 and 10 μm and $\sigma(A_E)$ was typically less than 10^{-5}. These fluctuations were small enough that their impact on

$\sigma(A_d)$ was negligible. Indeed, we believe that a significant contribution to the fluctuations in each monitor difference ΔM was the intrinsic measurement precision $\delta(\Delta M_i)$. We elaborate on this in section I B, where we discuss the monitoring instrumentation.

Another important consideration is the accuracy with which the coefficients β_i are measured. As mentioned earlier, these coefficients were evaluated using beam modulation, and will be discussed in Sect. **??**.

The above discussion regarding measurement accuracy and its impact on $\sigma(A_d)$ is particularly relevant in the monitoring of the electron beam properties such as beam intensity, trajectory and energy.

C. Spectrometers and Detectors

The Hall A high resolution spectrometers (HRS) at Jefferson Lab consist of a pair of identical spectrometers of QQDQ design, together with detectors for detecting the scattered particles [**?**]. The spectrometer and their standard detector package served to select for and to measure the kinematics quantities (x, Q^2) while suppressing other backgrounds originating from the target.

The spectrometers are designed to have a large acceptance with excellent resolution ($\Delta E/E \sim 10^{-4}$) and absolute accuracy in the reconstructed four–vectors of the events and, of less relevance for our experiment, precise normalization of the cross section. To measure Q^2 with sufficient accuracy requires good knowledge of the transfer matrix for the spectrometer to reconstruct events at the scattering point, as well as good pointing accuracy for the location of the spectrometers and precise measurements of beam position and angle. To calibrate the transfer matrix, a 0.5 mm thick tungsten plate with an array of pinholes is inserted in dedicated runs; reconstruction of the hole pattern determines the matrix.

1. Detector System

The scattered rate of electrons was determined by a trigger system in the HRS described in [**?**]. This trigger consisted of two scintillator planes, which provided the main timing trigger, a CO_2 gas cherenkov counter and a double-layered lead glass detector, which both provided particle identification information. The standard tracking detector (the vertical drift chamber) was turned off during production data taking because it may not endure the expected high event rates. During low-rate calibration runs, the tracking detector was turned on and the efficiency of the electron trigger and the pion rejection could be studied.

The signals for the gas cherenkov detector and the double-layered lead glass counter were passed through discriminators and logic units to form preliminary electron and pion triggers. These preliminary triggers are then combined with the scintillator triggers and cherenkov signals to form the final electron and pion triggers, which are then sent to scalers to record the event counts and form asymmetries. Particle identification is fulfilled by the use of discriminators for both the lead-glass and the cherenkov counters and proper settings of their thresholds.

For HRS the two layers of the leadglass counter are called "preshower" and "shower" detectors, respectively. The preshower blocks in the Right HRS (the spectrometer located to the right side of the beamline when viewed along the beam direction) has 48 blocks arranged in a 2×24 array, with the longest dimension of the blocks aligned perpendicular to the particle trajectory. For the two blocks in each row, only the ends facing outward are read out by photo-multiplier tubes (PMTs) and the other ends of the two blocks were facing each other and not read out. Therefore the preshower detector had 48 output channels. All preshower blocks were individually wrapped to prevent light leak. The preshower and the shower detectors in the Left HRS are similar to the preshower detector on the Right HRS except that for each detector there are 34 blocks arranged in a 2×17 array. The shower detector in the Right HRS had 75 blocks arranged in a 5×15 array with the longest dimension of the blocks aligned along the trajectory of scattered particles. PMTs are attached to each block of the Right shower detector on one end only, giving 75 output channels.

The particle identification (PID) was studied at low beam currents using fbTDC signals along with ADC spectrum of all detector signals recorded by the standard DAQ. Figure 2 shows the preshower vs. shower signals for group 2 on the Left HRS. A comparsion between no fbTDC cut and with cut on the fbTDC signal of the electron wide trigger from this group clearly shows the hardware PID cuts.

Electron efficiency and pion rejection factors of the lead glass counter on the Left HRS are shown in Fig. 3 as functions of the vertical hit position of the particle in the preshower detector. PID performance on the Right HRS is similar. Electron efficiency from wide groups are slightly higher than narrow groups because there is less event loss due to tim-

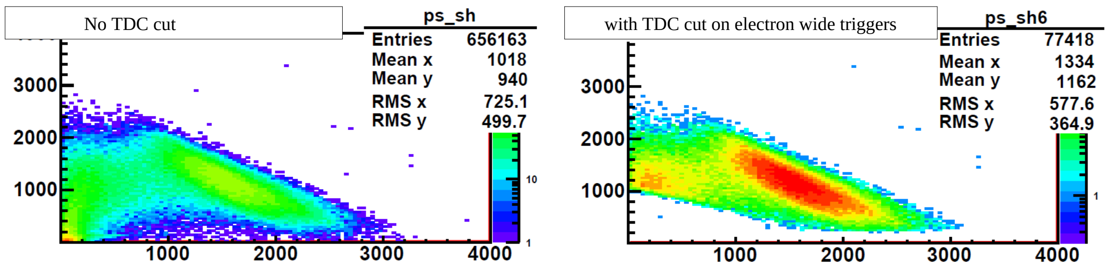

FIG. 2: Preshower vs. Shower ADC spectrum (sum of 8 blocks each) for group 2 on the Left HRS, without fbTDC cut (left) and with cut on the group 2 electron wide trigger fbTDC signal (right). It clearly shows the hardware cuts on the preshower and the total shower signals, indicating the DAQ is selecting the correct events as electrons. The cuts can be adjusted by changing the discriminator thresholds. The events near the vertical axis, around ADC channels (200,1000), are electrons that deposited energy in overlapping blocks between group 2 and group 1 (or group 3) and are recorded by the other group.

ing mis-alignment when taking the coincidence between the preshower and the total shower discriminator outputs. Variations in the electron efficiency across the spectrometer acceptance effectively change the kinematics (Q^2) of the measurement. For this reason, data were taken daily during the experiment to monitor the DAQ PID performance and corrections are applied to data.

Combined with the ≈ 200 pion rejection factor of the gas cherenkov counter, the total pion rejection was above 10^4. With the parity violation asymmetry of pion production being no larger than that of scattered electrons, the uncertainty in the final asymmetry results due to pion contamination is negligible compared to the $3-4\%$ statistical uncertainty.

2. *Data Acquisition System*

The signals from our trigger that define electrons and pions are sent to scalers (Struck Model 3801) where they are integrated over the helicity window. The scalers are part of the HAPPEX DAQ, which is a multiple-VME-crate DAQ system running under the CODA system developed at Jefferson Lab [?]. Signals from the various beam monitors are integrated and digitized by custom-built VME integrating ADCs. The system is triggered at the 30 Hz rate of the helicity reversal, synchronized to the end of each helicity window

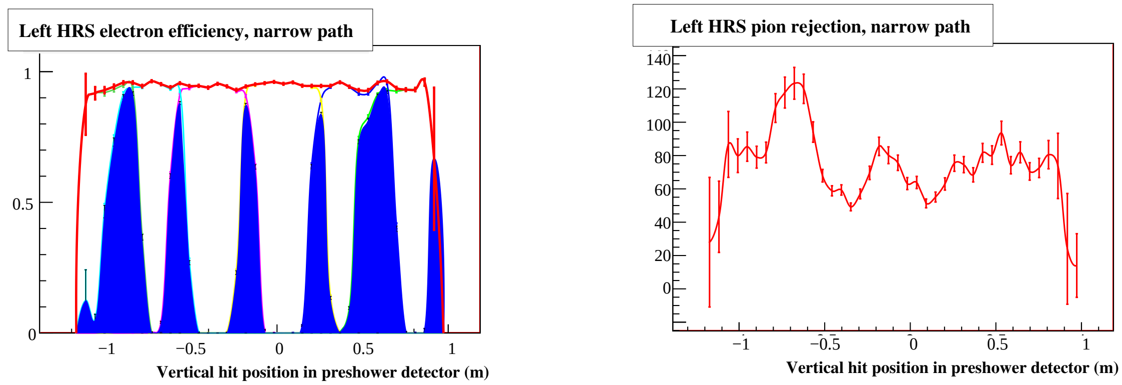

FIG. 3: Electron detection efficiency (left) and pion rejection factor (right) vs. vertical (dispersive) hit position of the particle in the preshower detector for the narrow electron triggers in the Left HRS. A one-hour run was used in this evaluation. For electron efficiencies, the total efficiency is shown by the red curve, while blue shaded area indicates events that are recorded by the two adjacent groups. The average electron efficiency across the detector for this one-hour run is $(94.626 \pm 0.002)\%$ and the averge pion rejection factor is 75.3 ± 1.1. The error bars are statistical only. PID performance for the wide path and the Right HRS are similar.

with the first 0.5 msec of the pulse blanked off to remove instabilities due to the switching of HV on the Pockels cell which controls the beam polarization. In addition to the scalers and ADCs, the DAQ reads input/output registers which record various information such as the helicity.

The scaler DAQ which counts triggers is designed to count event rates up to 1 MHz with hardware-based PID and with minimal deadtime of order 1%. The analysis of the deadtime is given in reference **??**. The detectors listed in section I C 1 provided the electron and pion triggers. A schematic of the trigger is shown in ref **??**.

D. Beam Polarimetry

The experimental asymmetry $A^{\rm exp}$ is related to the corrected asymmetry by

$$A^{\rm exp} = A_d^{\rm corr}/P_e \tag{5}$$

where P_e is the beam polarization. Three beam polarimetry techniques were available at JLab: A Mott polarimeter in the injector, and both a Møller and a Compton polarimeter in the experimental hall.

1. *Mott Polarimeter*

A Mott polarimeter [**?**] is located near the injector to the first linac, where the electrons have reached 5 MeV in energy. Mott polarimetry is based on the scattering of polarized electrons from unpolarized high-Z nuclei. The spin-orbit interaction of the electron's spin with the magnetic field it sees due to its motion relative to the nucleus causes a differential cross section

$$\sigma(\theta) = I(\theta)\left[1 + S(\theta)\vec{P}_e \cdot \hat{n}\right] \quad , \tag{6}$$

where $S(\theta)$ is the Sherman function and $I(\theta)$ is the spin-averaged scattered intensity

$$I(\theta) = \frac{Z^2 e^4}{4m^2\beta^4 c^4 \sin^4(\theta/2)}\left[1 - \beta^2 \sin^2(\theta/2)\right](1-\beta^2) \quad . \tag{7}$$

The unit vector $\hat{n}$ is normal to the scattering plane, defined by $\hat{n} = (\vec{k} \times \vec{k}')/|\vec{k} \times \vec{k}'|$ where $\vec{k}$ and $\vec{k}'$ are the electron's momentum before and after scattering, respectively. Thus $\sigma(\theta)$ depends on the electron beam polarization P_e. Defining an asymmetry

$$A(\theta) = \frac{N_L - N_R}{N_L + N_R} \; , \tag{8}$$

where N_L and N_R are the number of electrons scattered to the left and right, respectively, we have

$$A(\theta) = P_e \, S(\theta) \; , \tag{9}$$

and so knowledge of the Sherman function $S(\theta)$ allows P_e to be extracted from the measured asymmetry with a precision of 3% [**?**],[**?**]. The Mott polarimeter is also used for setting up and verifying the transversely-polarized beam used for systematic checks.

2. *Møller Polarimeter*

A Møller polarimeter measures the beam polarization via measuring the asymmetry in $\vec{e},\vec{e}$ scattering, which depends on the beam and target polarizations P^{beam} and P^{target}, as well as on the analyzing power A_m^{th} of Møller scattering:

$$A_m^{\mathrm{exp}} = \sum_{i=X,Y,Z} (A_{mi}^{\mathrm{th}} \cdot P_i^{\mathrm{targ}} \cdot P_i^{\mathrm{beam}}), \tag{10}$$

where $i = X, Y, Z$ defines the projections of the polarizations (Z is parallel to the beam, while $X - Z$ is the scattering plane). The analyzing powers $A^{\rm th}_{mi}$ depend on the scattering angle $\theta_{\rm CM}$ in the center-of-mass (CM) frame and are calculable in QED. The longitudinal analyzing power is

$$A^{\rm th}_{mZ} = -\frac{\sin^2\theta_{\rm CM}(7+\cos^2\theta_{\rm CM})}{(3+\cos^2\theta_{\rm CM})^2}. \tag{11}$$

The absolute values of $A^{\rm th}_{mZ}$ reach the maximum of 7/9 at $\theta_{\rm CM} = 90°$. At this angle the transverse analyzing powers are $A^{\rm th}_{mX} = -A^{\rm th}_{mY} = A^{\rm th}_{mZ}/7$.

The polarimeter target is a ferromagnetic foil magnetized in a magnetic field of 24 mT along its plane. The target foil can be oriented at various angles in the horizontal plane providing both longitudinal and transverse polarization measurements. The asymmetry is measured at two target angles ($\pm 20°$) and the average taken, which cancels transverse contributions and reduces the uncertainties of target angle measurements. At a given target angle two sets of measurements with oppositely signed target polarization are made which cancels some false asymmetries such as beam current asymmetries. The target polarization was $(7.95 \pm 0.24)\%$.

The Møller-scattered electrons were detected in a magnetic spectrometer consisting of three quadrupoles and a dipole [**?**]. The spectrometer selects electrons in a bite of $75° \leq \theta_{\rm CM} \leq 105°$ and $-5° \leq \phi_{\rm CM} \leq 5°$ where $\phi_{\rm CM}$ is the azimuthal angle. The detector consists of lead-glass calorimeter modules in two arms to detect the electrons in coincidence. More details about the Møller polarimeter are published in [**?**]. The total systematic error that can be achieved is 3.2% which is dominated by uncertainty in the foil polarization.

3. Compton Polarimeter

The Compton polarimeter [**?**] [**?**] [**?**] is based on scattering of the polarized electron beam from a polarized laser in a beam chicane. The backscattered photons are detected in a GsO crystal [**?**].

The experimental asymmetry $A^{\rm exp}_c = (N^+ - N^-)/(N^+ + N^-)$ is measured, where N^+ (N^-) refers to Compton counting rates for right (left) electron helicity, normalized to the beam intensity. This asymmetry is related to the electron beam polarization via

$$P_e = \frac{A^{\rm exp}_c}{P_\gamma A^{\rm th}_c} \tag{12}$$

where P_γ is the photon polarization and $A_c^{\rm th}$ the analyzing power. At typical JLab energies (a few GeV), the Compton cross-section asymmetry is only a few percent. To compensate for this, a Fabry-Perot cavity [**?**] is used to amplify the photon density of a standard low-power laser at the integration point. An average power of 1200 W is accumulated inside the cavity with a photon beam waist of the order of 150 μm and a photon polarization above 99%, monitored online at the exit of the cavity [**?**].

The accuracy of the compton polarimeter ... (show a figure of P_e vs time, and a table of systematics).

E. Target

The Hall A cryogenic target system [**?**] was used for this experiment. We used the a 20 cm deuterium target cell. The cell sits in an evacuated scattering chamber, along with subsystems for cooling, temperature and pressure monitoring, target motion, gas-handling, controls, and a solid and dummy target ladder.

The liquid deuterium loop was operated at a temperature of 19 K and a pressure of ~ 26 psia, leading to a density of about 0.0723 g/cm^3. The Al-walled target cells were 6.48 cm in diameter, and were oriented horizontally, along the beam direction. The upstream window thickness was 0.071 mm, the downstream window thickness was 0.094 mm, and the side wall thickness was 0.18 mm. Also mounted on the target ladder were solid thin targets of carbon, and aluminum dummy target cells, for use in background and spectrometer studies.

The target was mounted in a cylindrical scattering chamber of 104 cm diameter, centered on the pivot for the spectrometers. The scattering chamber was maintained under a 10^{-6} torr vacuum. The spectrometers view exit windows in the scattering chamber that were made of 0.406 mm thick Al foil.

To spread the heat load on the the target end-cap, the beam was rastered at 20 kHz by two sets of steering magnets 23 m upstream of the target. These magnets deflected the beam by up to ± 2.5 mm in x and y at the target. Local target boiling would manifest itself as an increase in fluctuations in the measured scattering rate, which would lead to an increase in the standard deviation of the pulse-pair asymmetries in the data, above that expected from counting statistics. Studies of the pulse-pair asymmetries for various beam currents and raster sizes were performed, at a lower Q^2 and thus at a higher scattering rate. Figure

?? shows the standard deviation of the pulse-pair asymmetries, extrapolated to full current values, for various beam currents and raster sizes. A significant increase over pure counting statistics, indicating local boiling effects, was observed only for the combination of a small raster (1.0 mm) size and large beam current (94 μA). During the experiment we used larger raster sizes for which there was little boiling noise.

II. DIS ASYMMETRY ANALYSIS

The physics asymmetries sought for in this experiment are 90 and 160 ppm, for the two Q^2 values, respectively. The measured asymmetries are about 10% smaller due to beam polarization. To understand the systematics of the asymmetry measurement, a half-wave plate (HWP) was inserted in the beamline to flip the laser helicity in the polarized source during half of the data taking period. The measured asymmetries flip sign for each beam HWP change and the magnitude of the asymmetry remain consistent within statistical error bars. The asymmetries are formed from event counts of each beam helicity pair (one pair has 33-ms of helicity plus and 33-ms of helicity minus beam), normalized by the beam charge. Figure **??** shows the pair-wise counting asymmetry from about 80% of the total data sets of this experiment. The different HWP states have already been corrected. One can see that the asymmetry spectrum agrees to four orders of magnitude with Gaussian distribution expected from purely statistical fluctuations.

A. Data Selection

Loose requirements were imposed on beam quality, removing periods of beam intensity, position, or energy instability, removing about 25% of the total data sample. No spin-direction-dependent cuts were applied. The dominant source of noise due to the beam arose from fluctuations in the beam current and beam energy.

As explained in detail in [31**?** , 32], the window-to-window differences in the asymmetry from beam jitter were reduced by using the correlations to beam position differences from precision beam position monitors, Δx_i by defining a correction $A_{beam} = \sum c_i \Delta x_i$. The c_i were measured several times each hour from calibration data where the beam was modulated using steering coils and an accelerating cavity. The largest c_i was for ^{208}Pb and was on the order of 50 ppb/nm. The spread in the resulting $A_n^m = A_{raw} - A_{beam}$ was observed to be dominated by counting statistics.

B. Pedestals and Linearity

The signals produced by the beam monitors and the detectors ideally are proportional to the actual rates in those devices. In reality, however, these signals can deviate from linearity over the full dynamic range and in general do not extrapolate to a zero pedestal.

To study the linearity of the detectors and cavity monitors, we compared them to an Unser monitor [**?**], a parametric current transformer which can be used as an absolute reference of current. For our purposes the Unser monitor's advantage is its excellent linearity at low currents which allows us to obtain the cavity monitor pedestals. However, the fluctuations in the Unser monitor's pedestals, which drift significantly on a time scale of several minutes, and the ordinarily small range of beam currents limited the precision of such comparisons during production data taking. Instead, we use calibration data in which the beam current is ramped up and down from zero to more than 50 μA. One cycle takes about a minute. The result is that for any given beam current we have about sixty samples spread over a half hour run. This breaks any random correlation between Unser pedestal fluctuations and beam current and converts the Unser pedestal systematic to a random error.

In order to study linearity, we make scatterplots of one signal versus another and fit each scatterplot to a straight line, using only events where 24 μA $< I_1 <$ 34 μA, a range in which exploratory fits suggested everything was fairly linear. We then examine the residuals between the scatterplots and the fits, relative to the signal size corresponding to about 32 μA, over the full range of beam current.

Figures 4 to 5 show the results as a function of I_1. In Fig. 4 we see the behavior of the two cavity monitors relative to the Unser monitor. Both show deviations from linearity below about 14 μA and above about 47 μA, though the high-current problem for I_1 is not as clear-cut as for I_2 and the nonlinearities are at worst about 1% of the signal.

In Fig. 5 we see residuals for fits of the two detector signals versus I_1. The nonlinear behavior at low current is due mainly to the cavity monitors. From 32 μA to over 50 μA the detectors are linear to well under 0.2%.

We may conclude that the detectors and cavity monitors are linear to well within the

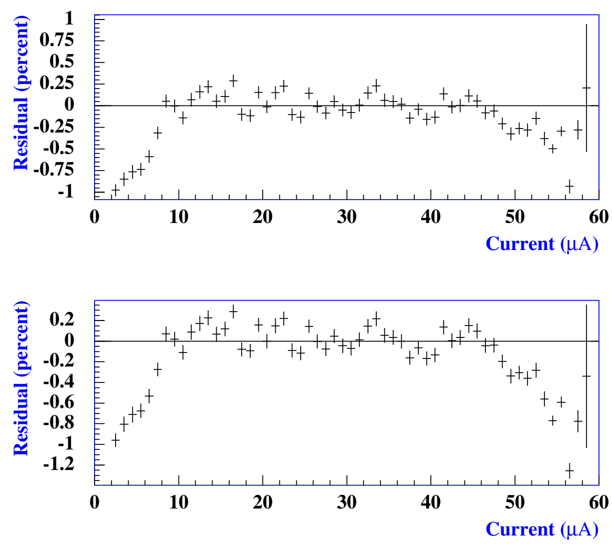

FIG. 4: (Color online) (top) Residuals from fit of BCM1 to Unser data, as a fraction of the BCM1 pulse height at 32 μA, versus beam current. (bottom) Same for fit of BCM2 to Unser.

required tolerances.

Detector pedestals were measured by averaging the detector signals during times when the beam is off. The resulting pedestals were always less than 0.3% of the signal corresponding to the lowest stable beam current in the production data set, and typically less than 0.06%; these pedestals are negligible.

The cavity monitor pedestals cannot be measured this way, since the cavity signals are meaningless when the beam is off. Instead, we fit $I_{1(2)}$ to I_U in the calibration data and extrapolate to zero current. Such an extrapolation requires knowledge of the average Unser pedestal, which is obtained from the beam-off data in the same run. The resulting pedestals are less than 2% of the signal corresponding to the lowest stable beam current in the production data set.

In conclusion, no corrections for pedestals or nonlinearities needed to be applied. The nonlinearities of the detectors and cavity monitors were negligible over the dynamic range of the beam current we ran. The pedestals for detectors and cavity monitors were negligible.

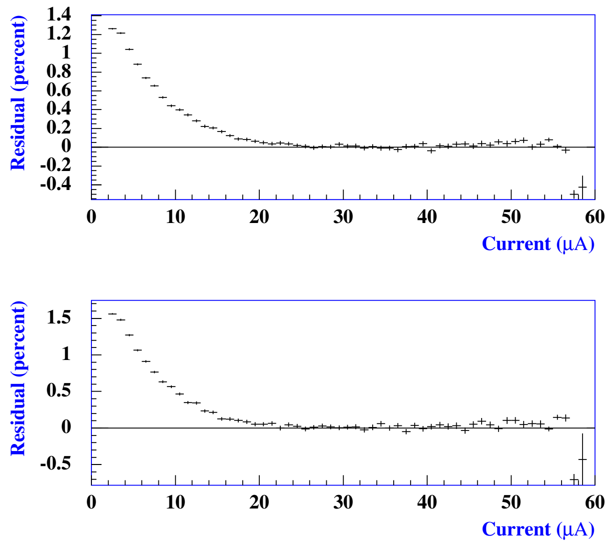

FIG. 5: (Color online) (top) Residuals from fit of detector 1 to BCM1 data, as a fraction of the detector 1 pulse height at 32 μA, versus beam current. (bottom) Same for fit of detector 2 to BCM1.

C. Systematic Fluctuations and Beam Corrections

Assuming that $\sigma(A_d)$ has negligible contributions from window-to-window beam fluctuations and instrumentation noise, there is still the possibility that there are helicity-correlated systematic effects at the sub-ppm level. If one considers the cumulative corrected asymmetry $A_d^{\rm corr}$ over many window pairs, one can write

$$\begin{aligned} A_d^{\rm corr} &\equiv \langle (A_d^{\rm corr})_i \rangle = \\ & \left\langle \left(\frac{\Delta D}{2D}\right)_i \right\rangle - \left\langle \left(\frac{\Delta I}{2I}\right)_i \right\rangle - \sum_j \beta_j \left\langle (\Delta M_j)_i \right\rangle \\ &= A_D - A_I - \sum_j A_{Mj}. \end{aligned} \quad (13)$$

For most of the running conditions during data collection, $A_d^{\rm corr} \simeq A_D \simeq 10$ ppm, which meant that all corrections were negligible. The cumulative average for A_I was maintained below 0.1 ppm. For A_{Mj}, the cumulative averages were found to be below 0.1 ppm during the run with the "bulk" GaAs photocathode. This resulted from the fact that the accelerator damped out position fluctuations produced at the source by a large factor (section **??**). The averaged position differences on target were kept below 10 nm.

However, during data collection with “strained” GaAs, position differences as large as several μm were observed in the electron beam at a point in the accelerator where the beam energy is 5 MeV. Continuous adjustment of the circular polarization of the laser beam was required to reduce the differences to about 0.5 μm. This resulted in observed position differences on target ranging from 10 nm to 100 nm, which in turn resulted in A_{Mj} in the range from 0.1 to 1 ppm.

The control of the asymmetry corrections within the aforementioned constraints was one of the central challenges during data collection. A variety of feedback techniques on the laser and electron beam properties were employed in order to accomplish this; these methods are discussed in Sec. **??**.

D. Background Analysis

1. Target EndCap Correction

Scattering from the target aluminum windows contributed $(0.5 \pm 0.1)\%$ (???) to our detected signal. This background was measured by inserting into the beam an empty aluminum target cell, similar to the one used to contain liquid deuterium, and measuring the signal in our detector. The thickness of the empty target cell walls is about 10 times that of the walls used in the deuterium cell, in order to compensate for the radiative losses in the deuterium cell.

The correction to our data arises from ... ??? ... explain the physics here; I guess if it’s DIS it’s then Aluminum is not much different from Deuterium ...

2. *Radiative Corrections*

3. *Pion Background Corrections*

E. Kinematics

1. *Calibration of The HRS Optics*

To calibrate the transfer matrix for the HRS, a 0.5 mm thick tungsten plate with an array of pinholes is inserted about 1 meter after the target and upstream of the first quadrupole of the HRS. The calibrations are dedicated runs at low rates with the vertical drift chambers (VDCs) turned on. Using the hole-pattern observed in the HRS focal plane, a chi-square minimization algorithm is performed to determine the matrix elements which transform the track vector to the location of the sieve slit.

Show some results from Kai Pan's analysis here.

2. *Reconstruction of Q^2 and x*

The four-momentum transfer squared is

$$Q^2 \;=\; 2\,E\,E'\,(1-\cos(\theta)) \tag{14}$$

where E is the incident energy, E' is the final momentum or energy of the electron ($E' \gg m_e$) and θ is the scattering angle.

For the beam energy we used the Tiefenbach energy (need to explain this) of ??? GeV and assumed a 3 MeV (???) average energy loss to the center of the target which is applied this as a correction to the beam energy. The error in the beam energy E and E' are assumed conservatively to be 3 MeV based on a history of these measurements in Hall A. The most important error is in θ ...

Perhaps need a table of errors.

III. PVDIS FORMALISM

This section discusses the formalism of parity-violating deep inelastic scattering. Extraction of the C_2 coefficients (section **??**) follow from this formalism.

$$A_{PV} \equiv \frac{\sigma_+ - \sigma_-}{\sigma_+ + \sigma_-} = \left(-\frac{G_F Q^2}{4\sqrt{2}\pi\alpha}\right)\left(2g_A^e Y_1 \frac{F_1^{\gamma Z}}{F_1^{\gamma}} + g_V^e Y_3 \frac{F_3^{\gamma Z}}{F_1^{\gamma}}\right) , \tag{15}$$

where Q^2 is the negative of the four-momentum transfer squared, G_F is the Fermi weak coupling constant, α is the fine structure constant, Y_1 and Y_3 are kinematic factors, and x is the Bjorken scaling variable. In the quark parton model,

$$F_1^{\gamma Z} = \sum g_V^q Q_q \left[q(x) + \bar{q}(x)\right] \tag{16}$$

$$F_3^{\gamma Z} = \sum g_A^q Q_q \left[q(x) - \bar{q}(x)\right] \tag{17}$$

$$F_1^{\gamma} = \frac{1}{2}\sum Q_q^2 \left[q(x) + \bar{q}(x)\right] \tag{18}$$

where Q_q is the electric charge of quarks and $q(x)$, $\bar{q}(x)$ are quark distribution functions. Rewriting $g^e_{A(V)} g^q_{V(A)}$ as $C_{1(2)q}$, and assuming $R^\gamma = R^{\gamma Z} = 0$, one has $Y_1 = 1$ and

$$A_{PV} = \left(\frac{3G_F Q^2}{\pi\alpha^2\sqrt{2}}\right) \times \frac{2C_{1u}[1 + R_C(x)] - C_{1d}[1 + R_S(x)] + Y_3(2C_{2u} - C_{2d})R_V(x)}{5 + R_S(x) + 4R_C(x)} , \tag{19}$$

where $R_{V,C,S}$ are related to quark distributions. The magnitude of the asymmetry is in the order of 10^{-4}, or 10^2 parts per million (ppm) at $Q^2 = 1$ (GeV/c)^2.

The tree-level Standard Model effective weak coupling constants $C_{1,2q}$ are

$$C_{1u} = 2g_A^e g_V^u = -\frac{1}{2} + \frac{3}{4}\sin^2\theta_W , \quad C_{2u} = 2g_V^e g_A^u = -\frac{1}{2} + 2\sin^2\theta_W ,$$
$$C_{1d} = 2g_A^e g_V^d = \frac{1}{2} - \frac{2}{3}\sin^2\theta_W , \quad C_{2d} = 2g_V^e g_A^d = \frac{1}{2} - 2\sin^2\theta_W ,$$

with θ_W the weak mixing angle. The goal of JLab E08-011 is to measure the PVDIS asymmetries to a statistical precision of 3% for the $Q^2 = 1.1\text{GeV}^2$ point and 4% for the the $Q^2 = 1.9\text{GeV}^2$ point. In addition, the systematic uncertainty goal is $< 3\%$, and under the assumption that hadronic physics corrections are small, our goal is to extract from these asymmetries the effective coupling constant combination $(2C_{2u} - C_{2d})$. The magnitude of the asymmetries is expected to be 90 and 170 ppm for the two measured kinematics of $Q^2 = 1.1$ and 1.9 (GeV/c)^2, respectively. To achieve the required precision, event rates up to 500 kHz are expected. Although this is not the first time the PVDIS asymmetries are measured, the only preceeding PVDIS measurement was carried out at SLAC [**? ?**] about 35 years ago, with a $\approx 9\%$ statistical and a $\approx 9\%$ systematic uncertainties. The increased precision of this experiment required better controls of all systematic uncertainties.

A. Simulation

Two simulation packages were used to support the analysis of this experiment. The package called "hamc" (Hall A Monte Carlo) was used to simulate the events and the spectrometer acceptance, while a second package called "hats" (Hall A Trigger Simulation) was used to simulate the response of the trigger used to identify electrons and pions, providing a calculation of our deadtime.

In "hamc", events are generated using a physics class that has information about the cross section and asymmetry. The tracks are generated uniformly in solid angle $d\Omega = sin(\theta)\, d\theta\, d\phi$ and the results later weighted by the differential cross section $\frac{d\sigma}{d\Omega}$. The simulated tracks undergo multiple scattering in the target and energy loss from the target from external and internal Brehmstrahlung as well as ionization loss,

The generated four-vectors are transported to the detector in the HRS focal plane using a set of polynomials that model the trajectories of electrons through the magnetic fields. The beam raster is simulated, which produces a smearing of the beam on target. The events are transported to intermediate apertures such as the collimator or the entrance to quadrupoles. Events that reach the HRS focal plane and intersect the detectors are integrated to compute the total rate and average asymmetry.

Here describe "hats" ...

B. Extraction of C_2 Coefficients

IV. DISCUSSION OF HIGHER TWIST EFFECTS

They are small.

---

[1] B. Frois *et al.*, Phys. Rev. Lett. **38**, 152 (1977).

[2] C. Garcia-Recio, J. Nieves, E. Oset, Nucl. Phys. A **547**, 473 (1992).

[3] L. Ray, W. R. Coker, G.W. Hoffmann, Phys. Rev. C **18**, 2641 (1978).

[4] V.E. Starodubsky, N.M. Hintz, Phys. Rev. C **49**, 2118 (1994).

[5] B.C. Clark, L.J. Kerr, S. Hama, Phys. Rev. C **67**, 054605 (2003).

[6] A. Trzcinska *et al.*, Phys. Rev. Lett. **87**, 082501 (2001).

[7] H. Lenske, Hyperfine Interact. **194**, 277 (2009).

[8] T.W. Donnelly, J. Dubach, I. Sick, Nucl. Phys.A **503**, 589 (1989).

[9] C.J. Horowitz, Phys. Rev. C **57** , 3430 (1998).

[10] C.J. Horowitz, S.J. Pollock, P.A. Souder, R. Michaels, Phys. Rev. C **63**, 025501 (2001).

[11] G.A. Lalazissis, J. Konig, P. Ring, Phys. Rev. C **55**, 540 (1997).

[12] B.G. Todd-Rutel, J. Piekarewicz, Phys. Rev. Lett. **95**, 122501 (2005).

[13] M. Beiner, H. Flocard, N. van Giai, P. Quentin, Nucl. Phys. A **238**, 29 (1975).

[14] E. Chabanat, P. Bonche, P. Haensel, J. Meyer, R. Schaeffer, Nucl. Phys. A **635**, 231 (1998).

[15] D. Vautherin, D. M. Brink, Phys. Rev. C **5**, 626 (1972).

[16] B.A. Brown, Phys. Rev. Lett. **85**, 5296 (2000).

[17] C.J. Horowitz, J. Piekarewicz, Phys. Rev. **C64**, 062802 (2001).

[18] F. Ozel, G. Baym, T. Guver, Phys. Rev. D **82**, 101301 (2010).

[19] A. W. Steiner, J. M. Lattimer, E. F. Brown, Astrophys. J. **722**, 33 (2010).

[20] K. Hebeler, J. M. Lattimer, C. J. Pethick, A. Schwenk, Phys. Rev. Lett. **105**, 161102 (2010).

[21] S. Gandolfi, J. Carlson, S. Reddy, arXiv:1101.1921.

[22] W. G. Lynch *et al.*, arXiv:0901.0412.

[23] M.B. Tsang *et al.*, Phys. Rev. Lett. **102**, 122701 (2009).

[24] C.J. Horowitz, J. Piekarewicz, Phys. Rev. C **66**, 055803 (2002).

[25] C.J. Horowitz, J. Piekarewicz, Phys. Rev. Lett. **86**, 5647 (2001).

[26] P. G. Reinhard, W. Nazarewicz, Phys. Rev. C **81**, 051303 (2010).

[27] A. Tamii et al., Phys. Rev. Lett. **107**, 062502 (2011).

[28] S. J. Pollock, E. N. Fortson, and L. Wilets, Phys. Rev. C **46**, 2587 (1992); S.J. Pollock and M.C. Welliver, Phys. Lett. B **464**, 177 (1999)

[29] B.A. Brown, A. Derevianko, V. V. Flambaum, Phys. Rev. C **79**, 035501 (2009).

[30] K. Tsigutkin *et al.*, Phys. Rev. A **81**, 032114 (2010).

[31] A. Acha *et al.*Phys. Rev. Lett. **98**, 032301 (2007).

[32] K. A. Aniol *et al.*Phys. Rev. Lett. **96**, 022003 (2006).

[33] K. A. Aniol *et al.*Phys. Rev. C **69**, 065501 (2004).

[34] J. Alcorn *et al.*, Nucl. Instrum. Meth. A **522**, 294 (2004).

[35] C. K. Sinclair, *et.al.* Phys. Rev. ST Accel. Beams 10, 023501 (2007); J. Hansknecht, *et.al.*

Phys. Rev. ST Accel. Beams 13, 010101 (2010).

[36] K. D. Paschke, Eur. Phys. J. A **32**, 549 (2007).

[37] A. Ong, J. C. Berengut, V. V. Flambaum, Phys. Rev. C **82**, 014320 (2010).

[38] S. Ban, C.J. Horowitz, R. Michaels, J. Phys G **39** (2012) 015104.

[39] X. Roca-Maza, M. Centelles, X. Vinas, M. Warda, Phys. Rev. Lett. **106**, 252501 (2011).